

RESEARCH ARTICLE

Curvature-based force estimation for an elastic tube

Qingyu Xiao¹ , Xiaofeng Yang² and Yue Chen^{1,*} 

¹Department of Biomedical Engineering, Georgia Institute of Technology/Emory University, Atlanta, GA, USA, 30332 and

²Department of Radiation Oncology, Emory University, Atlanta, GA, USA, 30322

*Corresponding author. E-mail: yue.chen@bme.gatech.edu

Received: 30 June 2022; **Revised:** 15 October 2022; **Accepted:** 26 December 2022; **First published online:** 13 February 2023

Keywords: continuum robots, force estimation, curvature

Abstract

Contact force is one of the most significant feedback for robots to achieve accurate control and safe interaction with environment. For continuum robots, it is possible to estimate the contact force based on the feedback of robot shapes, which can address the difficulty of mounting dedicated force sensors on the continuum robot body with strict dimension constraints. In this paper, we use local curvatures to estimate the magnitude and location of single or multiple contact forces based on Cosserat rod theory. We validate the proposed method in a thin elastic tube and calculate the curvatures via Fiber Bragg Grating (FBG) sensors or image feedback. For the curvature feedback obtained from multicore FBG sensors, the overall force magnitude estimation error is 0.062 ± 0.068 N and the overall location estimation error is 3.51 ± 2.60 mm. For the curvature feedback obtained from image, the overall force magnitude estimation error is 0.049 ± 0.048 N and the overall location estimation error is 2.75 ± 1.71 mm. The results demonstrate that the curvature-based force estimation method is able to accurately estimate the contact force.

1. Introduction

Continuum robots could easily change their configurations due to external contact, which will affect the robot motion and eventually alter the control efforts [1, 2]. The contact force is of great significance especially in medical settings such as cardiac ablation surgery, where the ablation area of the tissue largely depends on the contact force [3]. Many work has been done to estimate the contact forces. Contact force can be directly measured by embedding miniature force sensors on the robot body [4, 5]. However, these methods are only effective when the contact occurs at the sensor location, for instance at the tip of the robot. Also, the strict dimension constraints also limit the wide application of these approaches in needle-sized continuum robots, especially in the minimally invasive surgical tools where the tool tip often equipped with multiple treatment or diagnosis units [6, 7]. Alternatively, continuum robot task-space contact force can be estimated based on joint-space sensor measurement. For example, Bajo *et al.* [8, 9] proposed a method for tendon-driven continuum robot contact force sensing, but this requires a dedicated force cell at the actuation unit. The joint-space force cells may not be available for some continuum devices such as concentric tubes [10], steerable needles [11], or in MR-guided interventions [12–15] where the MRI-conditional force sensor is not readily available.¹

Alternatively, force can be estimated implicitly based on the measurements of continuum robot configuration change. This is applicable since the intrinsic compliant nature of continuum robots allows the robot configuration to be changed with the contact forces [16]. Many models have been proposed to predict the continuum robot shape based on contact force, including beam-based method [17], calibration method [18], variable curvature method [19], and Cosserat rod theory [20]. Contact forces, in turn, can be estimated by matching the measured shape with model shape.

Related works have been published to estimate the contact force using shape-based method, which compares the difference between measured shape and model shape in the point cloud. Qiao [21]

proposed a shape-based method to estimate contact forces by minimizing the difference between the measured shape and model shape with Kalman filters. However, the estimation error is relatively large, with force mean error of 30.59% and locations mean error of 17.20%. Aloï [22] proposed a shape-based method using Fourier transformation. This method will estimate the force in a distributed fashion and can detect the force location by observing the "peaks" of the distributed force profile. However, it cannot provide useful information on the exact force magnitude and location if it is point contact.

Aside from shape-based method, curvatures can provide more robust information for force estimation. This is because the curvatures remain invariant for any translations or rotations the continuum robot undergoes. The curvatures along the continuum robot can be measured using multicore fiber Bragg grating (FBG) sensors [23, 24] or intraoperative images with curvature estimation algorithms [25–29]. Several curvature-based methods have been investigated for force estimation. Qiao [30] utilized FBGS to measure the curvatures along the manipulator and calculated the force (mean error of 9.8% error) and locations (mean error of 3.6% error) directly using constitutive law. Al-Ahmad [31] utilized an unscented Kalman filter to the measured curvatures, which achieved 7.3% error of force magnitude and 4.6% error of location. However, the estimated location error is still large because these methods cannot solve subnode accuracy and require expensive FBG sensors embedded in the instrument.

In this paper, we present a curvature-based force estimation method that enables force estimation in a subnode accuracy. We also illustrate curvature-based method has advantages over shape-based method regarding the loss map convexity. Moreover, a local frame representation of Cosserat rod theory is derived to achieve faster curvature computation, which avoids the time-consuming integration of rotation matrix. Aside from obtaining the curvature feedback from FBG sensors, we also investigate the feasibility of obtaining the curvature from image feedback using the line integral method. The result shows that the contact force locations and magnitudes can be accurately estimated by curvature from both FBG sensors and images. The contributions of this paper include:

- Distributed the contact force to adjacent nodes to solve the model in subnode accuracy.
- Derived a local frame representation of Cosserat rod theory to achieve faster computation.
- Investigated the method to compute local curvature based on image feedback.
- Experimentally validated the proposed estimation method on single and multiple contact force cases.

The structure of the paper is arranged as follows. Section 2 describes the derivation of a local frame representation of Cosserat rod theory for curvature calculation. Section 3 discusses the method to solve the model in subnode accuracy and the methods to compute the feedback curvatures from multicore FBG sensors and the images. Section 4 shows the experimental results of the force estimation regarding the force magnitudes and the locations. Finally, Section 5 is the conclusion.

2. Model curvature calculation

2.1. Review of Cosserat rod model

Cosserat rod model describes the equilibrium state of a small segment of thin rod subjected to internal and external distributed forces and moments. Previous works [32] have detailed the differential geometry of a thin rod with Cosserat rod theory so that the deformation can be estimated by solving Ordinary differential equations (ODEs) in (1)–(4) given external forces F_e and external moments L_e . To distinguish variables from different frames, we use lowercase letters for variables in local frame and uppercase letters for variables in global frame.

$$\dot{P} = Rv \quad (1)$$

$$\dot{R} = R\hat{u} \quad (2)$$

$$\dot{N} = -F_e \quad (3)$$

$$\dot{\mathbf{M}} = -\dot{\mathbf{P}} \times \mathbf{N} - \mathbf{L}_e \tag{4}$$

where the dot symbol in $\dot{\mathbf{x}}$ represents the derivative of \mathbf{x} respect to the arc length s , hat symbol in $\hat{\mathbf{x}}$ reconstruct vector \mathbf{x} to a 3 by 3 skew symmetric matrix, \mathbf{P} is the shape in global frame, R is the rotation matrix of local frame relative to the global frame, \mathbf{N} and \mathbf{M} are internal force and moment in global frame which obeys the constitutive law

$$\mathbf{N} = RK_{SE} (\mathbf{v} - \mathbf{v}^*) \tag{5}$$

$$\mathbf{M} = RK_{BT} (\mathbf{u} - \mathbf{u}^*) \tag{6}$$

\mathbf{v} and \mathbf{u} are differential geometry parameters of a rod, \mathbf{v}^* and \mathbf{u}^* are differential geometry parameters of a rod with no external loads. K_{SE} and K_{BT} are the stiffness matrices. The boundary conditions for solving the ODEs (1)–(4) are described as

$$\mathbf{N} (loc_{tip}) = \mathbf{F}_{tip} \tag{7}$$

$$\mathbf{M} (loc_{tip}) = \mathbf{T}_{tip} \tag{8}$$

where \mathbf{F}_{tip} and \mathbf{T}_{tip} are external force and torque applied at the tip. loc_{tip} is the tip position in arc length. Thus, the rod shape \mathbf{P} can be computed by solving the boundary value problem (BVP).

2.2. ODEs for model curvature calculation

The widely accepted Cosserat rod model in (1)–(4) are expressed in global frame. But it is beneficial to use the model in local frame to calculate the curvatures. We firstly take the derivative of \mathbf{M} in (6) and combine with (4)

$$R\hat{\mathbf{u}}K_{BT} (\mathbf{u} - \mathbf{u}^*) + RK_{BT}\dot{\mathbf{u}} = -\dot{\mathbf{P}} \times \mathbf{N} - \mathbf{L}_e \tag{9}$$

Then, using the relation $\dot{\mathbf{P}} \times \mathbf{N} = \hat{\mathbf{P}}\mathbf{N}$, $\dot{\mathbf{P}} = R\mathbf{v}$, and $(\hat{R}\mathbf{v}) = R\hat{\mathbf{v}}R^T$ (this is true when $R \in SO(3)$), we can obtain

$$R\hat{\mathbf{u}}K_{BT}(\mathbf{u} - \mathbf{u}^*) + RK_{BT}\dot{\mathbf{u}} = -R\hat{\mathbf{v}}R^T\mathbf{N} - \mathbf{L}_e \tag{10}$$

Multiplying R^T on both side, and solve for $\dot{\mathbf{u}}$, we can have

$$\dot{\mathbf{u}} = -K_{BT}^{-1} (\hat{\mathbf{u}}K_{BT}(\mathbf{u} - \mathbf{u}^*) + \hat{\mathbf{v}}R^T\mathbf{N} + R^T\mathbf{L}_e) \tag{11}$$

We define local variables $\mathbf{n} = R^T\mathbf{N}$, and $\mathbf{l}_e = R^T\mathbf{L}_e$. The meaning of the variables \mathbf{n} and \mathbf{l}_e are actually the variables \mathbf{N} and \mathbf{L}_e expressed in local frame, respectively. Hence, (11) becomes

$$\dot{\mathbf{u}} = -K_{BT}^{-1} (\hat{\mathbf{u}}K_{BT}(\mathbf{u} - \mathbf{u}^*) + \hat{\mathbf{v}}\mathbf{n} + \mathbf{l}_e) \tag{12}$$

In order to solve \mathbf{n} , we use (3) and multiply R^T on the two sides and add $\dot{R}^T\mathbf{N}$, which gives

$$R^T\dot{\mathbf{N}} + \dot{R}^T\mathbf{N} = -R^T\mathbf{F}_e + \dot{R}^T\mathbf{N} \tag{13}$$

Again, we define $R^T\mathbf{F}_e = \mathbf{f}_e$. Notice that the left-hand side in (13) is actually the derivative of $R^T\mathbf{N}$, which is $\dot{\mathbf{n}}$. \dot{R} can be replaced by (2) on the right-hand side. Thus, we have

$$\dot{\mathbf{n}} = -\mathbf{f}_e + \hat{\mathbf{u}}\mathbf{n} \tag{14}$$

To sum up, the curvatures of a general rod can be calculated by

$$\dot{\mathbf{u}} = -K_{BT}^{-1} (\hat{\mathbf{u}}K_{BT}(\mathbf{u} - \mathbf{u}^*) + \hat{\mathbf{v}}\mathbf{n} + \mathbf{l}_e) \tag{15}$$

$$\dot{\mathbf{n}} = -\mathbf{f}_e + \hat{\mathbf{u}}\mathbf{n} \tag{16}$$

with boundary conditions

$$\mathbf{u}(loc_{tip}) = \mathbf{0} \tag{17}$$

$$\mathbf{n}(loc_{tip}) = \mathbf{f}_{tip} \tag{18}$$

where loc_{tip} and \mathbf{f}_{tip} are the location and applied external force at the tip, respectively. (15) and (16) can be simplified in a special case where the rod is straight ($\mathbf{u}^* = \mathbf{0}$ and $\mathbf{v}^* = [0 \ 0 \ 1]^T$), with circular cross-section ($K_{11} = K_{22} = K_{33}/2$), nonshear and inextensible ($\mathbf{v} = [0 \ 0 \ 1]^T$), and no external moment ($\mathbf{l}_e = \mathbf{0}$). The simplified ODEs can be written as

$$\dot{u}_x = -n_y/K_{BT,11} \tag{19}$$

$$\dot{u}_y = n_x/K_{BT,22} \tag{20}$$

$$\dot{n}_x = -f_x + u_y n_z \tag{21}$$

$$\dot{n}_y = -f_y - u_x n_z \tag{22}$$

$$\dot{n}_z = -f_z - u_y n_x + u_x n_y \tag{23}$$

where x , y , and z are the first, second, and third component of a vector, respectively. $K_{BT,ij}$ means the entry of K_{BT} at row i and column j . And (21)–(23) is the same as (16). Note that both the integral variables and the boundary conditions are defined in local frame, the curvature u_x and u_y can be solved by simple backward integration from the distal point ($s = L$) to the proximal point ($s = 0$), which requires no iterative computation to solve a standard BVP. Therefore, the computational complexity is only determined by the number of nodes we divide along the arc length. Moreover, solving (19)–(23) will lead to the same result as solving the model in (1)–(4), but the former method will have faster performance for curvature calculation.

3. Force estimation approach

3.1. Point forces for Cosserat model

The force defined in Cosserat rod theory is distributed force whose unit is N/m. However, the objective of this paper is to estimate the magnitude and location of point force whose unit is N. Conversion has to be performed between point force and distributed force. Firstly, we define the applied point forces in a new force vector which contains the locations and magnitude components of all forces.

$$\mathbf{f}_{vec} = [s^1, f_{pt,x}^1, f_{pt,y}^1, s^2, f_{pt,x}^2, f_{pt,y}^2, \dots, s^h, f_{pt,x}^h, f_{pt,y}^h]^T \tag{24}$$

where s^i is the location of the i^{th} point force, $f_{pt,x}^i$ and $f_{pt,y}^i$ are the components of the i^{th} point force, and h is the total number of forces acting on the continuum robot. The arc length of the manipulator can be divided into $q - 1$ segments, and this gives

$$\mathbf{Loc} = [loc_1, loc_2, \dots, loc_q] \tag{25}$$

where loc_i is the location of the i^{th} node, \mathbf{Loc} is the whole list of the nodes. In order to achieve subnode accuracy, we convert the point forces to distributed forces \mathbf{f}_{vec} on the nodes \mathbf{Loc} . Figure 1 shows an example to distribute the point force f_{pt}^i to two adjacent nodes $j - 1$ and j , the point force is distributed linearly according to the arc length distance between the two nodes. Therefore, the distributed forces can be calculated by

$$f^{j-1} = \frac{f_{pt}^i}{(loc_j - loc_{j-1})^2} (s^i - loc_{j-1}) \tag{26}$$

$$f^j = \frac{f_{pt}^i}{(loc_j - loc_{j-1})^2} (loc_j - s^i) \tag{27}$$

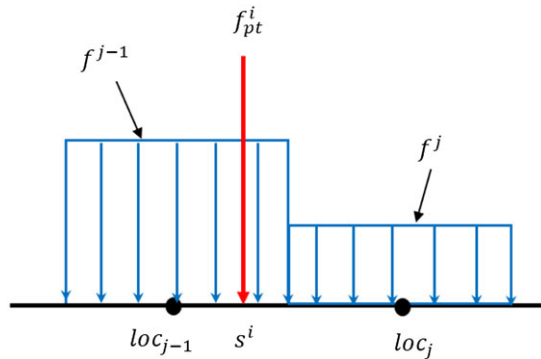


Figure 1. Distribution of point force to adjacent nodes to achieve subnode accuracy.

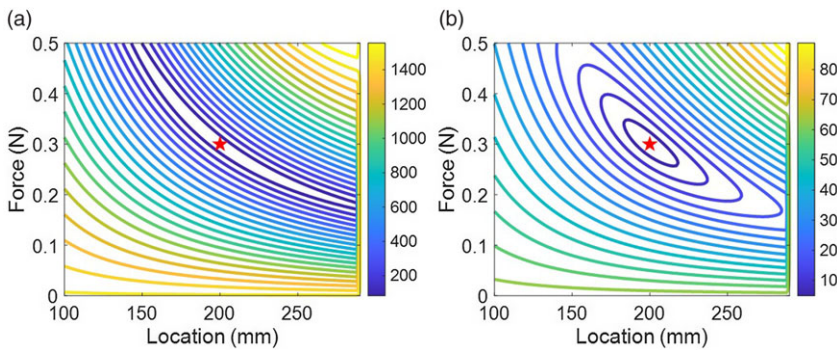


Figure 2. Loss maps computed by (a) shape (b) curvature.

where f^j (N/m) is the distributed force, f_{pt}^i (N) is the point force, loc_{j-1} and loc_j are two adjacent nodes for s^i . Note that the s^i is located between the nodes loc_{j-1} and loc_j , which allows the model to solve the solution in subnode accuracy. In the case where multiple point forces are close and distributed to the same node, the forces on that node will be superposed. After knowing the distributed forces along the rod, the mechanics model is complete and curvature can then be calculated through the integration of (19)–(23).

3.2. Curvature-based force estimation

A robust method for force estimation is to minimize the least square loss between the calculated curvature with measured curvatures.

$$loss_u(\mathbf{f}_{vec}) = \|\mathbf{u}_{cal} - \tilde{\mathbf{u}}\|^2 \tag{28}$$

where \mathbf{u}_{cal} is the curvature calculated from \mathbf{f}_{vec} and $\tilde{\mathbf{u}}$ is the curvature measured by sensors.

Similar to minimizing the loss of curvature, the loss of shape $loss_p(\mathbf{f}_{vec})$ could also be used for the objective function of the optimization algorithm. Figure 2 shows a simulation example of the loss of shape $loss_p(\mathbf{f}_{vec})$ and loss of curvature $loss_u(\mathbf{f}_{vec})$ with various force magnitudes and locations. The loss map is calculated by following steps: 1) Choosing $\mathbf{f}_{vec} = [200 \ 0.3 \ 0]^T$ as the ground truth, and calculate the curvature $\tilde{\mathbf{u}}$ and shape $\tilde{\mathbf{p}}$ using Cosserat rod theory. The $\tilde{\mathbf{u}}$ and $\tilde{\mathbf{p}}$ can be assumed as the measured data from sensors. 2) Calculate \mathbf{u}_{cal} and \mathbf{p}_{cal} with the same method, but use different \mathbf{f}_{vec} whose first component ranges from 100 to 290 mm and the second component ranges from 0 to 0.5 N. 3) Use (28) to compute the loss for each pair of force magnitude and location. As illustrated in Fig. 2, the loss of

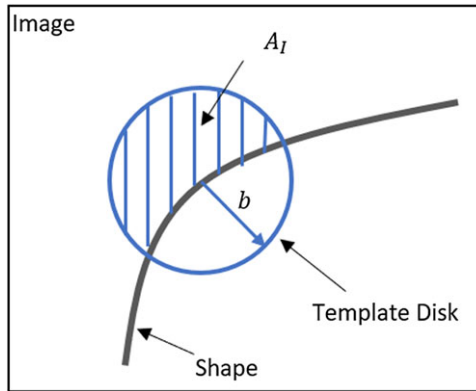


Figure 3. Compute the curvatures using template disk. A_I is the area surrounded by the template disk and the shape, and b is the radius of the template disk.

curvature (b) shows better convex property than that of shape coordinates (a), and thus more robust results can be calculated [33]. Therefore, we use curvature-based method to estimate the force.

3.3. Curvature feedback

Curvature feedback of a elastic tube can be obtained from either FBG sensors or images. For curvature measurement using FBG sensors, multicore FBG fiber is typically used to compute the curvature through the change of the Bragg wavelength [34]. In this paper, the curvature measurement using FBG sensors is obtained directly from the software *Shape Sensing v1.3.1* provided by the supplier.

To obtain the curvature feedback from the intraoperative image feedback, one of the major challenges is that the shape of the tube on the image is noisy, especially when the resolution of the image is low. This is because the tube shape can only be discretely captured by pixels of the image and the resulting centerline of the tube is not continuous. Thus, it is inapplicable to compute the curvature based on the basic geometry, which is the norm of the derivative of the tangent direction. The derivative of a noisy shape will increase the noise magnitude and reduce the quality of the curvature feedback. Many methods have been proposed to reduce the noise of the curvature feedback from the image feedback, including segmentation methods [27, 28] and integral invariant methods [26, 29]. In this paper, we implemented the integral invariant method proposed in ref. [25] to compute the curvature feedback of the elastic tube from an image, which can be described as

$$\|\mathbf{u}\| \approx \frac{3A_I}{b^3} - \frac{3\pi}{2b} \quad (29)$$

where $\|\mathbf{u}\|$ is the norm of the curvature feedback at the center of the template disk, A_I is the area surrounded by the template disk and the shape, and b is the radius of the template disk (see Fig. 3). However, this integral invariant method can only be used to compute the curvature feedback of a tube if the tube only has in-plane bending. Special care has to be taken to compute the curvature feedback from image of a tube with out-of-plane bending, which will be the focus of our future work.

4. Experiments and results

In this section, we will validate the curvature-based force estimation method on single, double, and triple point force cases, with the curvature measured from FBG sensors or calculated via image feedback.

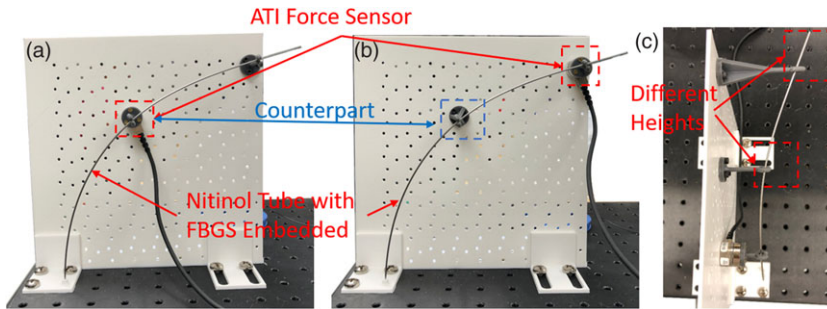


Figure 4. Experiment setup for force estimation. The ATI force sensor with a probe is mounted on a fixed vertical wall. The FBGS is inserted inside Nitinol tube for curvature measurement. Counterpart of each force sensor with probe are designed to keep the shape of Nitinol in (a) and (b) the same, and the force sensor can swap the location. Different height design of the probe in (c) allows for 3D shape deformation.

4.1. Force estimation result using multicore FBG sensors

4.1.1. Experiment setup

As illustrated in Fig. 4, the experiments were performed by adding multiple forces to a straight Nitinol tube. ATI force sensor (ATI Industrial Automation, United States) with 3D printed probe was mounted on a fixed vertical board. The probes are designed with different height in order to contact the Nitinol tube at various location and orientation (Fig. 4(c)). For every single probe that mounted on the force sensor, a counterpart probe (Fig. 4(a) and (b)) is also designed to keep the same distance from the probe head to the wall. This allows the force sensor with probe to be interchangeable with its counterpart such that the shape of Nitinol tube shape remains unchanged. For example, the Nitinol tube in Fig. 4(a) and (b) has the same shape, but the location of the force sensor is swapped. Thus, we can use one force sensor to measure multiple external forces. Fiber Bragg gratings sensors (FBGS International NV, Belgium) was inserted inside the Nitinol tube to measure the curvature.

4.1.2. System parameter calibration

The system calibration was conducted in two steps: (1) location calibration and (2) stiffness calibration. Since the FBGS fiber is transparent, it is hard to identify the locations of gratings inside the fiber. But the relative locations (spacing between adjacent gratings) are specified on the user manual (20 mm). The objective of location calibration is to ensure the curvatures we measured are aligned with the positions on the Nitinol. Three cases of single force at different locations were recorded, and the bias of the location can be minimized by adding an offset to the results.

$$s_{est} = s_{cal} + s_{bias} \quad (30)$$

where s_{est} is the estimated location of the external force, s_{cal} is the result of the model, and s_{bias} is the bias to offset the error. After location calibration, we conducted stiffness calibration to match the calculated force magnitude with the measured force magnitude. Notice that the stiffness change has trivial impact on the location estimation, therefore the location calibration is still valid after completing the stiffness calibration. The result of the calibration is listed in Table I.

4.1.3. Force estimation results

The error analysis of the force estimation result is grouped into three categories: single force estimation analysis, double forces estimation analysis, and triple forces estimation analysis. For each category, the experiment was performed 13 times by applying varying contact force (0.27–1.96 N) at 13 different

Table I. Calibrated parameters.

Name	Variable	Value	Unit
Nitinol tube length	loc_{tip}	290	mm
Inner tube diameter	d_{in}	1.118	mm
Outer tube diameter	d_{out}	1.397	mm
Young's modulus	E_{ni}	67	GPa
Location bias	s_{bias}	-3.12	mm

Table II. Force estimation RMSE using FBG sensor feedback.

Estimation		1 force	2 forces	3 forces	Overall
Magnitude (N)	mean	0.037	0.060	0.127	0.062
	std	0.069	0.046	0.081	0.068
Location (mm)	mean	2.95	2.58	4.69	3.51
	std	2.17	2.06	4.06	2.60

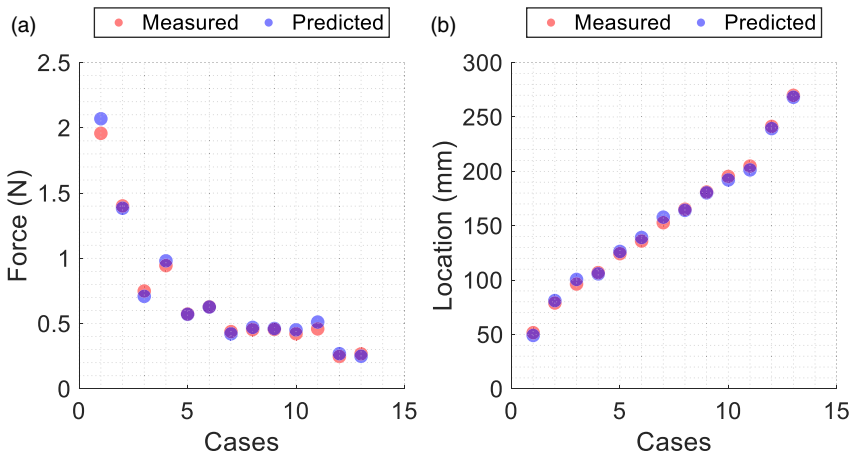


Figure 5. Experimental results for single force estimation. (a) Force magnitude estimation. (b) force location estimation.

locations on the Nitinol tube. The step size of the integration of the ODEs for curvature calculation is $ds = 1$ mm.

As summarized in Table II, the RMSE of single force estimation, double force estimation, and triple force estimation are 0.037 ± 0.069 N, 0.060 ± 0.046 N, and 0.127 ± 0.081 N, respectively. Therefore, the proposed method can estimate the force magnitude accurately, despite the fact that larger number of forces can slightly reduce the estimation accuracy on force magnitude. The RMSE of the single-location estimation, double-location estimation, and triple-location estimation is 2.95 ± 2.17 mm, 2.58 ± 2.06 mm, and 4.69 ± 4.06 mm, respectively. This indicates that a larger location error will occur when the number of external forces increases.

Figures 5 and 6 summarize the force estimation results for single force and multiple forces, respectively. The blue dots are the predicted result and the red dots are the measured results. Most of the cases in Fig. 5 can be predicted accurately except case 1 (error magnitude of 8.72%). This error occurs because the curvature can only be measured by the first few gratings (the spacing of adjacent gratings is 20 mm), while the rest gratings will read 0 because no internal moment exists after the location where the force is applied. In Fig. 6, each case has two or three values, which refer to the two or three forces, respectively.

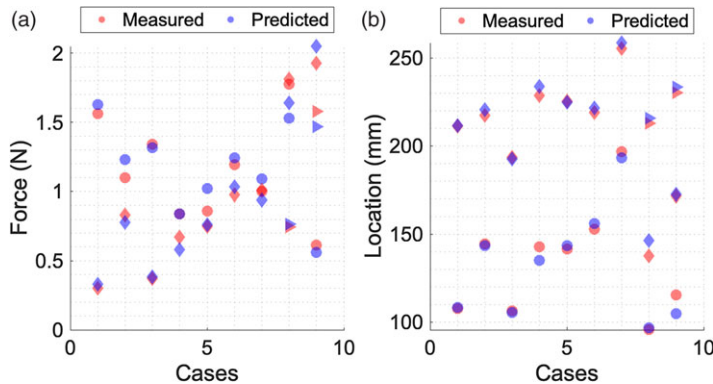


Figure 6. Experimental results for double and triple forces estimation. (a) Force magnitudes estimation. (b) force locations estimation. During each experiment, the circle marker indicates the first force, diamond marker indicates the second force, and the triangle marker indicates the third force (triple force scenario).

The red dots and the blue dots are aligned well with each other, which demonstrates the accuracy of the proposed estimation method.

4.2. Force Estimation result using image feedback

In this subsection, we investigate the potential application of curvature-based force estimation method in image-guided interventions. We assume the continuum robot with in-plane bending so that its shape can be captured by one image. However, the 3D shape reconstruction of the continuum robot with out-of-plane bending can be achieved by images captured from multiple viewing angles or 3D imaging techniques such as MRI [35] or 3D ultrasound imaging [36].

4.2.1. Workflow to estimate the force from images

The process to estimate the contact force can be summarized as: (a) continuum robot centerline detection; (b) compute the curvature feedback based on the detected centerline; and (c) estimate the contact force based on the curvature feedback. Here, we assume the continuum robot shape can be accurately identified via various image segmentation techniques [37] or mounting active tracking coils on the continuum device [12, 38]. Thus, we will skip the image segmentation step in this preliminary study. To obtain this ideal continuum robot shape from image feedback, we first deform the Nitinol tube with random force, overlay the deformed tube (Fig. 7(a)) on a 128×170 grid with the pixel resolution of $0.5 \text{ mm} \times 0.5 \text{ mm}$ (which is the ultrasound imaging resolution), and then threshold the grid (as shown in Fig. 7(b)) to obtain Fig. 7(c). After obtaining continuum tube image, the centerline of the continuum robot, as presented in Fig. 7(d) can be detected. This will be achieved by the skeletonization algorithm proposed in refs. [39, 40], which is well-accepted imaging processing algorithm in the field of computer vision. A sample continuum robot image and the corresponding result of the skeletonization algorithm are presented in Fig. 7(d). After detecting the centerline of the continuum robot, the curvature feedback of the robot can then be computed through (29). Finally, the contact force can be estimated by the curvature-based force estimation method by feeding the curvature feedback we computed.

4.2.2. Force estimation results

As presented in Fig. 8, the curvature feedback can be computed accurately from image data. This is a critical step for the curvature-based force estimation method. After obtaining the curvature feedback, we use them to estimate the force magnitudes and the corresponding locations. The step size of the

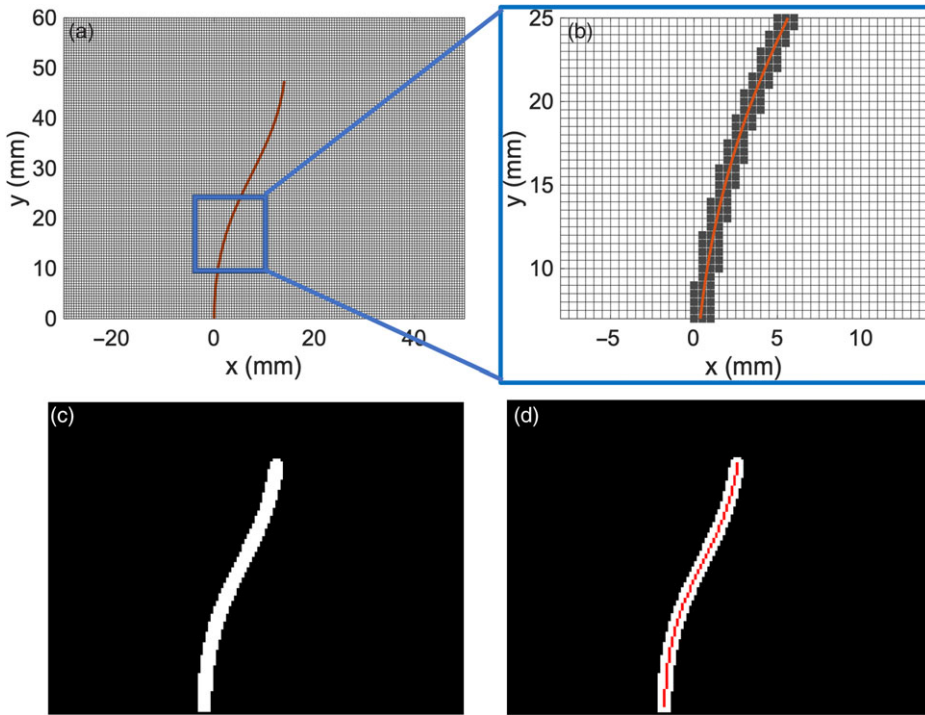


Figure 7. (a) Shape of the deformed rod. (b) The blurred grid within the threshold. (c) The resulting image of the deformed rod. (d) Centerline (red pixels) detection using skeletonization algorithm.

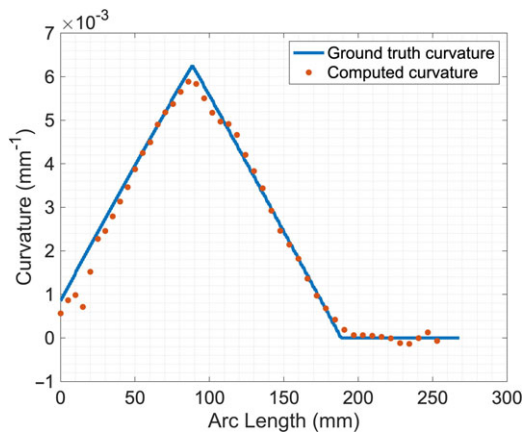


Figure 8. Curvatures computed from the imaging.

integration of the ODEs for curvature calculation is $ds = 1$ mm. The results of the curvature-based force estimation are presented in Figs. 9 and 10. As summarized in Table III, the overall force magnitude estimation error is 0.049 ± 0.048 N and the overall location estimation error is 2.75 ± 1.71 mm. For single force estimation, the force magnitude estimation error is 0.045 ± 0.040 N and the location error is 2.20 ± 1.73 mm. For double force estimation, the force magnitude estimation error is 0.051 ± 0.048 N and the location estimation error is 3.11 ± 1.64 mm. For triple force estimation, the force magnitude estimation error is 0.050 ± 0.037 N and the location estimation error is 2.59 ± 1.41 mm. The result shows that the curvature-based method can estimate the force locations accurately for either single force or multiple force estimations. However, the force magnitude accuracy will be degraded if more forces

Table III. Force estimation RMSE using image feedback.

Estimation		1 force	2 forces	3 forces	Overall
Magnitude (N)	mean	0.045	0.051	0.050	0.049
	std	0.040	0.048	0.037	0.048
Location (mm)	mean	2.20	3.11	2.59	2.75
	std	1.73	1.64	1.41	1.71

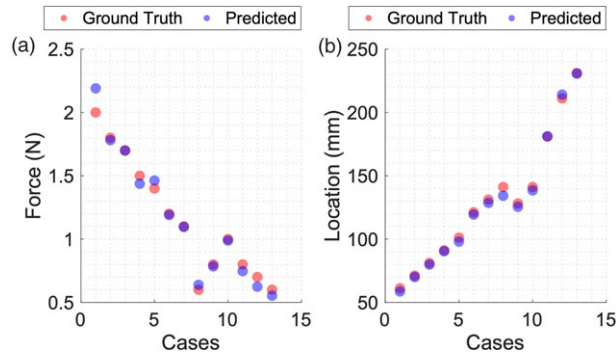


Figure 9. Single force estimation result based on curvature computed from image. (a) Force magnitude estimation. (b) Force location estimation.

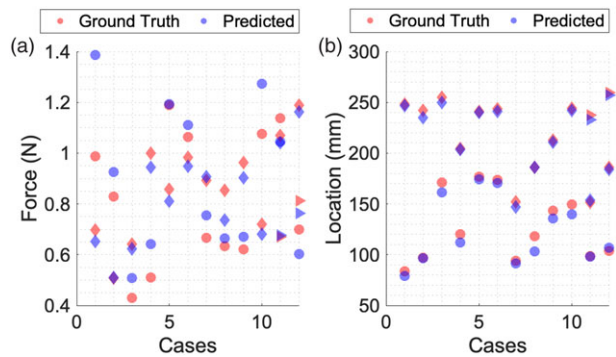


Figure 10. Experimental results for double and triple forces estimation based on image feedback. (a) Force magnitudes estimation. (b) Force locations estimation. During each experiment, the circle marker indicates the first force, diamond marker indicates the second force, and the triangle marker indicates the third force (triple force scenario).

are acting on the rod. Although moderate errors exist, this result validates the feasibility of applying curvature-based force estimation method with image data to estimate the contact force.

5. Conclusions

In this article, we develop the curvature-based force estimation method to estimate the contact force magnitude and location. The proposed method was validated on a straight 290 mm Nitinol tube, with single or multiple forces acting at different locations. The curvature feedback was obtained from the multicore FBG sensors and the images. The results showed that the model can estimate the force magnitude and location accurately. For the curvature feedback obtained from multicore FBG sensors, the overall force magnitude estimation error is 0.062 ± 0.068 N and the overall location estimation error is 3.51 ± 2.60

mm. For the curvature feedback obtained from image, the overall force magnitude estimation error is 0.049 ± 0.048 N and the overall location estimation error is 2.75 ± 1.71 mm.

However, the accurate force estimation relies on reliable curvature calculation of the deformed continuum robot. One of the main challenges for practical implementation is to accurately extract the center line from multiple images when robot is subjected to 3D deformation. 3D shape reconstruction may have larger noise or error caused by multicamera calibration. Moreover, computing the curvature from 3D reconstructed shape remains a challenging task. Therefore, our future work will involve the study of 3D contact force estimation, machine learning methods for curvature calculation, and evaluation of the force estimation performance in clinical settings with 3D image feedback such as 3D ultrasound and magnetic resonance imaging.

Author contributions. Qingyu Xiao, Xiaofeng Yang, and Yue Chen designed the study. Qingyu Xiao conducted data gathering. Qingyu Xiao and Yue Chen wrote the article.

Financial support. This research was partially funded by Georgia Institute of Technology Startup Grant.

Conflict of interest. Not applicable.

Ethical standards. Not applicable.

References

- [1] Y. Chen, L. Wang, K. Galloway, I. Godage, N. Simaan and E. Barth, "Modal-based kinematics and contact detection of soft robots," *Soft Robot.* **8**(3), 298–309 (2021).
- [2] Q. Xiao, M. Musa, I. S. Godage, H. Su and Y. Chen, "Kinematics and stiffness modeling of soft robot with a concentric backbone," *J. Mech. Robot.* **15**(5), 051011 (2023).
- [3] S. B. Kesner and R. D. Howe, "Robotic catheter cardiac ablation combining ultrasound guidance and force control," *Int. J. Robot. Res.* **33**(4), 631–644 (2014).
- [4] M. Mitsuishi, N. Sugita and P. Pitakwatchara, "Force-feedback augmentation modes in the laparoscopic minimally invasive telesurgical system," *IEEE/ASME Trans. Mechatron.* **12**(4), 447–454 (2007).
- [5] P. Valdastri, K. Harada, A. Menciassi, L. Beccai, C. Stefanini, M. Fujie and P. Dario, "Integration of a miniaturised triaxial force sensor in a minimally invasive surgical tool," *IEEE Trans. Biomed. Eng.* **53**(11), 2397–2400 (2006).
- [6] A. Alipour, E. S. Meyer, C. L. Dumoulin, R. D. Watkins, H. Elahi, W. Loew, J. Schweitzer, G. Olson, Y. Chen, S. Tao and M. Guttman, "MRI conditional actively tracked metallic electrophysiology catheters and guidewires with miniature tethered radio-frequency traps: theory, design, and validation," *IEEE Trans. Biomed. Eng.* **67**(6), 1616–1627 (2019).
- [7] A. L. Gunderman, E. J. Schmidt, A. N. Viswanathan, H. R. Halperin, J. Tokuda, R. T. Seethamraju and Y. Chen, "Mr-Guided Tissue Puncture with On-line Imaging for High-resolution Theranostics," *In: 2020 International Symposium on Medical Robotics (ISMR)* (IEEE, 2020) pp. 57–61.
- [8] A. Bajo and N. Simaan, "Finding Lost Wrenches: Using Continuum Robots for Contact Detection and Estimation of Contact Location," *In: 2010 IEEE International Conference on Robotics and Automation* (IEEE, 2010) pp. 3666–3673.
- [9] A. Bajo and N. Simaan, "Kinematics-based detection and localization of contacts along multisegment continuum robots," *IEEE Trans. Robot.* **28**(2), 291–302 (2011).
- [10] Y. Chen, M. E. Poorman, D. B. Comber, E. B. Pitt, C. Liu, I. S. Godage, H. Yu, W. A. Grissom, E. J. Barth and R. J. Webster III, "Treating Epilepsy Via Thermal Ablation: Initial Experiments with an Mri-Guided Concentric Tube Robot," *In: Frontiers in Biomedical Devices*. vol. 40672 (American Society of Mechanical Engineers, 2017) pp. V001T02A002.
- [11] Y. Chen, I. S. Godage, S. Sengupta, C. L. Liu, K. D. Weaver and E. J. Barth, "Mr-conditional steerable needle robot for intracerebral hemorrhage removal," *Int. J. Comput. Ass. Rad.* **14**(1), 105–115 (2019).
- [12] Y. Chen, J. Howard, I. Godage and S. Sengupta, "Closed loop control of an mr-conditional robot with wireless tracking coil feedback," *Ann. Biomed. Eng.* **47**(11), 2322–2333 (2019).
- [13] A. Gunderman, E. Schmidt, M. Morcos, J. Tokuda, R. T. Seethamraju, H. Halperin, A. Viswanathan and Y. Chen, "Mr-tracked deflectable stylet for gynecologic brachytherapy," *IEEE/ASME Trans. Mechatron.* **27**(1), 407–417 (2021).
- [14] A. L. Gunderman, S. Sengupta, E. Siampli, D. Sigounas, C. Kellner, C. Oluigbo, K. Sharma, I. Godage, K. Cleary and Y. Chen, "A surgical platform for intracerebral hemorrhage robotic evacuation (aspahre): A non-metallic mr-guided concentric tube robot, arXiv preprint arXiv: 2206.09848 (2022).
- [15] K. W. Kwok, K. H. Lee, Y. Chen, W. Wang, Y. Hu, G. C. Chow, H. S. Zhang, W. G. Stevenson, R. Y. Kwong, W. Luk and E. J. Schmidt, "Interfacing fast multi-phase cardiac image registration with MRI-based catheter tracking for MRI-guided electrophysiological ablative procedures," *Circulation* **130**(Suppl. 2), A18568–A18568 (2014).
- [16] R. J. Webster III and B. A. Jones, "Design and kinematic modeling of constant curvature continuum robots: A review," *Int. J. Robot. Res.* **29**(13), 1661–1683 (2010).

- [17] A. Stilli, E. Kolokotronis, J. Fraś, A. Ataka, K. Althoefer and H. A. Wurdemann, "Static Kinematics for An Antagonistically Actuated Robot Based on a Beam-mechanics-based Model," *In: 2018 IEEE/RSJ International Conference on Intelligent Robots and Systems (IROS)* (IEEE, 2018) pp. 6959–6964.
- [18] L. Wang and N. Simaan, "Geometric calibration of continuum robots: Joint space and equilibrium shape deviations," *IEEE Trans. Robot.* **35**(2), 387–402 (2019).
- [19] T. Mahl, A. Hildebrandt and O. Sawodny, "A variable curvature continuum kinematics for kinematic control of the bionic handling assistant," *IEEE Trans. Robot.* **30**(4), 935–949 (2014).
- [20] D. C. Rucker, B. A. Jones and R. J. Webster III, "A geometrically exact model for externally loaded concentric-tube continuum robots," *IEEE Trans. Robot.* **26**(5), 769–780 (2010).
- [21] Q. Qiao, G. Borghesan, J. De Schutter and E. V. Poorten, "Force from shape—Estimating the location and magnitude of the external force on flexible instruments," *IEEE Trans. Robot.* **37**(5), 1826–1833 (2021).
- [22] V. A. Aloï and D. C. Rucker, "Estimating Loads Along Elastic Rods," *In: 2019 International Conference on Robotics and Automation (ICRA)* (IEEE, 2019) pp. 2867–2873.
- [23] C. Gouveia, P. A. S. Jorge, J. M. Baptista and O. Frazao, "Temperature-independent curvature sensor using FBG cladding modes based on a core misaligned splice," *IEEE Photonic. Tech. Lett.* **23**(12), 804–806 (2011).
- [24] R. Xu, A. Yurkewich and R. V. Patel, "Curvature, torsion, and force sensing in continuum robots using helically wrapped fbg sensors," *IEEE Robot. Automat. Lett.* **1**(2), 1052–1059 (2016).
- [25] O. I. Frette, G. Virnovsky and D. Silin, "Estimation of the curvature of an interface from a digital 2D image," *Comp. Mater. Sci.* **44**(3), 867–875 (2009).
- [26] W.-Y. Lin, Y.-L. Chiu, K. R. Widder, Y. H. Hu and N. Boston, "Robust and accurate curvature estimation using adaptive line integrals," *Eurasip. J. Adv. Sig. Process.* **1**(1), 2010–2014 (2010).
- [27] T. P. Nguyen and I. Debled-Rennesson, "Curvature Estimation in Noisy Curves," *In: International Conference on Computer Analysis of Images and Patterns* (Springer, 2007) pp. 474–481.
- [28] T. P. Nguyen and I. Debled-Rennesson, "Curvature and Torsion Estimators for 3D Curves," *In: International Symposium on Visual Computing* (Springer, 2008) pp. 688–699.
- [29] H. Pottmann, J. Wallner, Y.-L. Yang, Y.-K. Lai and S.-M. Hu, "Principal curvatures from the integral invariant viewpoint," *Comput. Aided Geom. Des.* **24**(8-9), 428–442 (2007).
- [30] Q. Qiao, D. Willems, G. Borghesan, M. Ourak, J. De Schutter and E. V. Poorten, "Estimating and Localizing External Forces Applied on Flexible Instruments by Shape Sensing," *In: 2019 19th International Conference on Advanced Robotics (ICAR)* (IEEE, 2019) pp. 227–233.
- [31] O. Al-Ahmad, M. Ourak, J. Vlekken and E. V. Poorten, "Fbg-based estimation of external forces along flexible instrument bodies," *Front. Robot. AI* **8**, 718033 (2021).
- [32] B. A. Jones, R. L. Gray and K. Turlapati, "Three Dimensional Statics for Continuum Robotics," *In: 2009 IEEE/RSJ International Conference on Intelligent Robots and Systems* (IEEE, 2009) pp. 2659–2664.
- [33] S. Bubeck, "Convex optimization: Algorithms and complexity, arXiv preprint arXiv: 1405.4980 (2014).
- [34] J. P. Moore and M. D. Rogge, "Shape sensing using multi-core fiber optic cable and parametric curve solutions," *Opt. Exp.* **20**(3), 2967–2973 (2012).
- [35] K.-W. Kwok, Y. Chen, T. C. P. Chau, W. Luk, K. R. Nilsson, E. J. Schmidt and T. T. Zion, "Mri-based visual and haptic catheter feedback: simulating a novel system's contribution to efficient and safe mri-guided cardiac electrophysiology procedures," *J. Cardio. Magn. Reson.* **16**(1), 1–3 (2014).
- [36] X. Dai, Y. Lei, J. Roper, Y. Chen, J. D. Bradley, W. J. Curran, T. Liu and X. Yang, "Deep learning-based motion tracking using ultrasound images," *Aip. Conf. Proc.* **48**(12), 7747–7756 (2021).
- [37] R. A. Manakov, D. Y. Kolpashchikov, V. V. Danilov, I. P. S. Nikita Vitalievich Laptev and O. M. Gerget, "Visual Shape and Position Sensing Algorithm for a Continuum Robot," *In: IOP Conference Series: Materials Science and Engineering* (IOP Publishing, vol. 1019, 2021) pp. 012066.
- [38] T. T. Z. Yue Chen, W. Wang, R. Y. Kwong, W. G. Stevenson and E. J. Schmidt, "Intra-cardiac mr imaging & mr-tracking catheter for improved mr-guided ep," *J. Cardio. Magn. Reson.* **17**(1), 1–2 (2015).
- [39] M. Kerschitzki, P. Kollmannsberger, M. Burghammer, G. N. Duda, R. Weinkamer, W. Wagermaier and P. Fratzl, "Architecture of the osteocyte network correlates with bone material quality," *J. Bone Miner. Res.* **28**(8), 1837–1845 (2013).
- [40] T.-C. Lee, R. L. Kashyap and C.-N. Chu, "Building skeleton models via 3-D medial surface axis thinning algorithms," *CVGIP: Graph. Models Image Process.* **56**(6), 462–478 (1994).